Journal of Radiological Protection

Official journal of the Society for Radiological Protection

PAPER • OPEN ACCESS

Dosimetric and microdosimetric analyses for blood exposed to reactor-derived thermal neutrons

To cite this article: F Ali *et al* 2018 *J. Radiol. Prot.* **38** 1037

OPEN ACCESS
IOP Publishing | Society for Radiological Protection Journal of Radiological Protection
J. Radiol. Prot. **38** (2018) 1037–1052 (16pp) https://doi.org/10.1088/1361-6498/aaca9f

Dosimetric and microdosimetric analyses for blood exposed to reactor-derived thermal neutrons

F Ali[1], J Atanackovic[4], C Boyer[2], A Festarini[3], J Kildea[5], L C Paterson[1], R Rogge[2], M Stuart[3] and R B Richardson[1,5]

[1] Radiobiology and Health Branch, Canadian Nuclear Laboratories, Chalk River, ON, K0J 1J0, Canada
[2] Neutron Scattering Branch, Canadian Nuclear Laboratories, Chalk River, ON, K0J 1J0, Canada
[3] Environmental Sciences Branch, Canadian Nuclear Laboratories, Chalk River, ON, K0J 1J0, Canada
[4] Ontario Power Generation–Health Physics Laboratory, Whitby, ON, L1N 9E3, Canada
[5] McGill Medical Physics Unit, Cedars Cancer Centre–Glen Site, Montreal, QC, H4A 3J1, Canada

E-mail: richard.richardson@cnl.ca

Received 12 February 2018, revised 24 May 2018
Accepted for publication 6 June 2018
Published 21 June 2018

Abstract

Thermal neutrons are found in reactor, radiotherapy, aircraft, and space environments. The purpose of this study was to characterise the dosimetry and microdosimetry of thermal neutron exposures, using three simulation codes, as a precursor to quantitative radiobiological studies using blood samples. An irradiation line was designed employing a pyrolytic graphite crystal or—alternatively—a super mirror to expose blood samples to thermal neutrons from the National Research Universal reactor to determine radiobiological parameters. The crystal was used when assessing the relative biological effectiveness for dicentric chromosome aberrations, and other biomarkers, in lymphocytes over a low absorbed dose range of 1.2–14 mGy. Higher exposures using a super mirror will allow the additional quantification of mitochondrial responses. The physical size of the thermal neutron fields and their respective wavelength distribution was determined using the McStas Monte

Carlo code. Spinning the blood samples produced a spatially uniform absorbed dose as determined from Monte Carlo N-Particle version 6 simulations. The major part (71%) of the total absorbed dose to blood was determined to be from the $^{14}N(n,p)^{14}C$ reaction and the remainder from the $^{1}H(n,\gamma)^{2}H$ reaction. Previous radiobiological experiments at Canadian Nuclear Laboratories involving thermal neutron irradiation of blood yielded a relative biological effectiveness of 26 ± 7. Using the Particle and Heavy Ion Transport Code System, a similar value of $\sim$19 for the quality factor of thermal neutrons initiating the $^{14}N(n,p)^{14}C$ reaction in soft tissue was determined by microdosimetric simulations. This calculated quality factor is of similar high value to the experimentally-derived relative biological effectiveness, and indicates the potential of thermal neutrons to induce deleterious health effects in superficial organs such as cataracts of the eye lens.

Keywords: thermal neutrons, quality factor, blood, microdosimetry

(Some figures may appear in colour only in the online journal)

1. Introduction

Polyenergetic neutron fields present in a variety of environments possess a significant thermal neutron component. Examples of such fields are those in CANDU® reactor workplaces [1], radiotherapy environments [2], and inside aircraft at high altitudes [3], where neutron fields have similar characteristics to those in space (figure 1).

Research has been undertaken at the National Research Universal (NRU) reactor to understand the radiobiological effects in blood when exposed to thermal neutron radiation, (nominally 25 meV) with energies ranging from 7 to 327 meV, as described later. An irradiation line was constructed to guide thermal neutrons that passed through a sapphire crystal and collimated apertures to minimise gamma rays and fast neutron contaminants incident on the blood samples. The neutron fluence rate was routinely assessed by gold foil and independent beam monitor measurements accounting for reactor power. Initial low dose exposures in the range of 1.2–14 mGy using an in-line pyrolytic graphite (PG) crystal allowed the assessment of chromosomal aberrations in lymphocytes from blood (Paterson [4]). In the simulation environment, the PG crystal was replaced by a super mirror which allowed higher neutron fluence and dose rates of thermal neutrons for the measurements in lymphocytes of biological health indicators and the determination of changes to rapidly dividing mitochondria. Sets of Monte Carlo simulations were undertaken for two computer-driven configurations, using (i) the PG crystal or, alternatively, (ii) a super mirror of multiple layers of nickel and titanium. Each scattering device served to provide a thermal neutron beam impinging on the blood. The cylindrical tube, specially designed and constructed at Canadian Nuclear Laboratories (CNL) to contain the blood, consisted of a quartz tube designed to hold approximately 4.59 grams of blood with a nominal inner diameter of 10.5 mm and a blood-height of 50 mm. During each irradiation, the tubes were slowly rotated to flatten the spatial distribution of the absorbed dose within the blood sample.

Three Monte Carlo simulation codes were used to provide a comprehensive characterisation of these thermal neutron irradiations of blood. The spatial size and wavelength distribution resulting from the PG crystal and super mirror inserts was calculated by the McStas code [5] . For both the PG crystal and super mirror, the spatial distribution of dose to the

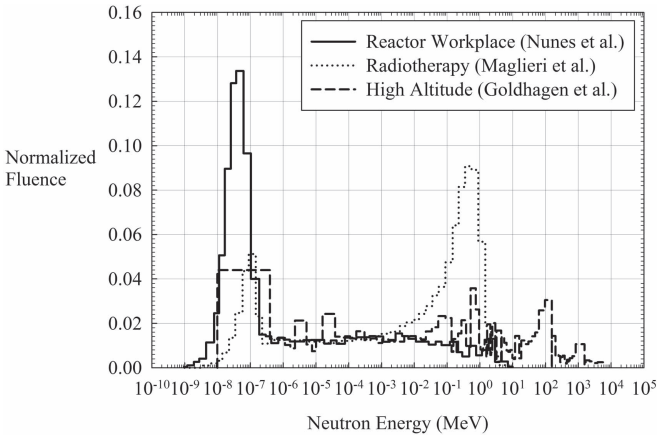

Figure 1. Normalised neutron energy spectra in reactor, radiotherapy, and high altitude environments.

rotating blood volume, along with the dose from secondary gamma rays produced in the wall and blood, was calculated using Monte Carlo N-Particle 6 version 1.0 (MCNP6) [6]. The microdosimetric mean quality factor of thermal neutrons was quantified using the Particle and Heavy Ion Transport code System (PHITS) [7] version 2.64 when the PG crystal and super mirror were used. Note that all simulation code runs employed a minimum of 10^8 source particles, with MCNP6 reporting a tally error of $<0.1\%$.

This article in section 2 characterises the thermal neutron fields incident on the blood samples. Section 3 calculates the spatial distribution of absorbed dose and secondary gamma ray kerma delivered to a blood sample, section 4 calculates the microdosimetric mean quality factor of thermal neutrons, and section 5 describes the relevance of this study to the dosimetry of eye lens and other targets.

2. Beam line characterisation simulations

The neutron source term used has a Maxwellian wavelength distribution, ranging from 0.049 nm to 0.35 nm, with a temperature of 300 K. For thermal neutron irradiation of blood, the dominant mechanism through which dose is delivered is the $^{14}N(n,p)^{14}C$ primary capture reaction [8], which has a Q-value of 625.87 keV [9]. $^{14}N(n,p)^{14}C$ dominance is due to the cross sections for nuclear capture reactions, leading to secondary charged particle emission, with the other isotopes in blood being zero at thermal neutron energies. It is assumed that the ^{14}N mass fraction in blood is 2.96% [10].

Scattering was achieved with a PG crystal, width of 121 mm and height of 60 mm, d-spacing of 0.3355 nm, and rotated at 20.69° to the incident beam line. Using Bragg's law [11], it was determined that neutron radiation with an average wavelength of 0.237 nm was scattered towards the blood sample midpoint located 985 mm from the PG crystal, creating a 30 mm by 60 mm field size (figure 2).

The resultant wavelength distribution has four peaks, centred at 0.235 nm, 0.115 nm, 0.078 nm, and 0.059 nm which correspond to first, second, third, and fourth order scattering respectively (figure 3). Using this wavelength distribution, the relative number-weighted average neutron kinetic energy incident on the blood sample is found to be 64 meV. Using the

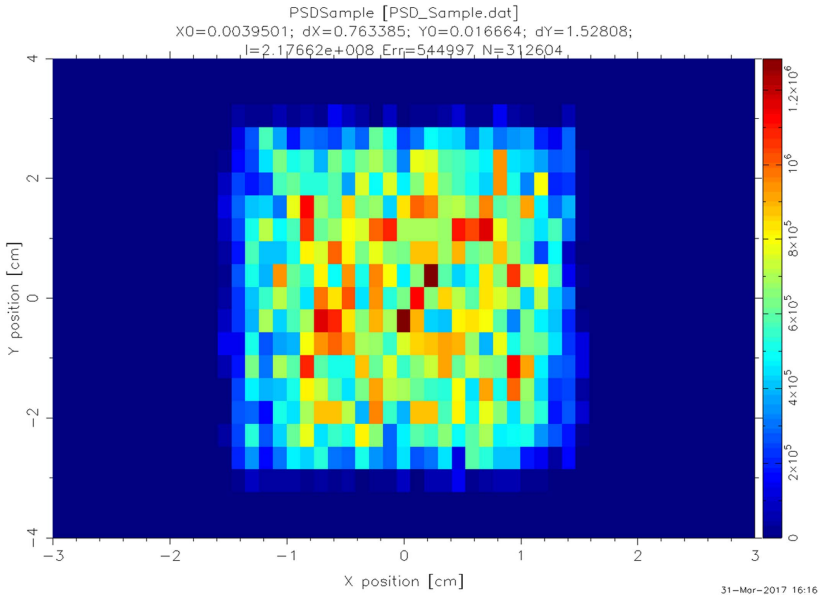

Figure 2. Spatial extent and intensity (red, more intense) of scattered thermal neutron field incident on blood sample with PG crystal inserted into incident beam line, simulated with McStas.

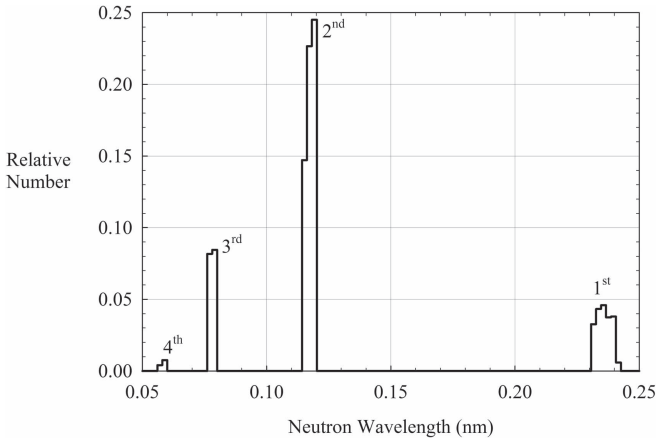

Figure 3. First four orders of scattered neutron wavelength distribution incident on blood sample with PG crystal inserted into incident beam line (abscissa range 0.05 nm, 327 meV to 0.25 nm, 13 meV).

wavelength distribution in figure 3, the absorbed dose per unit of neutron fluence incident on the blood volume is estimated to be 0.18 pGy cm^2 n^{-1} (excluding secondary gamma contributions from $^1H(n,\gamma)^2H$ capture reactions).

The super mirror has a width and height of 400 mm and 60 mm respectively, an *m*-value of 5, a reflectivity of 0.72, and is rotated at 0.9° to the line of incidence. The scattered neutron

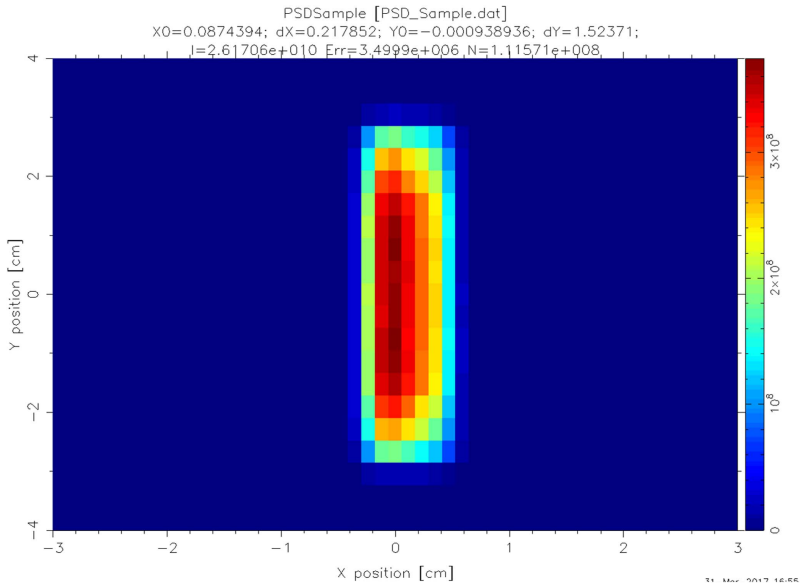

Figure 4. Spatial extent and intensity (red, more intense) of scattered thermal neutron field incident on blood sample with super mirror inserted into beam line, simulated with McStas.

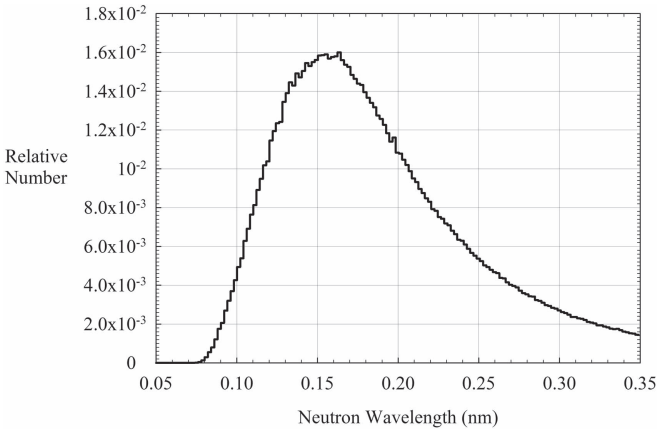

Figure 5. Scattered neutron wavelength distribution incident on blood sample with super mirror inserted into incident thermal neutron beam line (abscissa range 0.05 nm, 327 meV to 0.35 nm, 7 meV).

field, which irradiates the blood sample located 985 mm from the super mirror, is 10 mm wide by 60 mm high (figure 4).

The super mirror produces a much wider wavelength distribution of scattered neutrons on the blood sample, in comparison to the PG crystal (figure 5).

The relative number-weighted average neutron kinetic energy is 31 meV, and the absorbed dose per unit neutron fluence delivered to the 4.59 g blood volume is

Table 1. Neutron absorbed dose and secondary gamma ray kerma and tertiary electron absorbed dose, delivered to overall blood volume, per unit neutron fluence. For neutron and tertiary electron absorbed dose coefficients, the values listed in parentheses are their percentage contribution to the total absorbed dose coefficient.

Quantity (pGy cm^2 n^{-1})	PG crystal		Super mirror	
	Stationary	Rotational	Stationary	Rotational
Analytical calculations (*using* figures 3 and 5)				
Neutron absorbed dose per unit neutron fluence	0.180		0.250	
MCNP6 Calculations				
$^{14}N(n,p)^{14}C$ absorbed dose per unit neutron fluence[a]	0.194 (70.55%)	0.194 (70.80%)	0.234 (70.69%)	0.234 (70.69%)
$^{1}H(n,\gamma)^{2}H$ secondary gamma ray kerma per unit neutron fluence[b]	0.130	0.130	0.158	0.158
Tertiary electron (from $^{1}H(n,\gamma)^{2}H$) absorbed dose per unit neutron fluence[c]	0.081 (29.45%)	0.080 (29.20%)	0.097 (29.31%)	0.097 (29.31%)
[d]Total absorbed dose per unit neutron fluence	0.275	0.274	0.331	0.331

[a] F4/FM4 tally.
[b] F6 tally.
[c] *F8 tally.
[d] Sum of neutron and tertiary electron values.

0.25 pGy cm^2 n^{-1} (excluding secondary gamma contributions from $^{1}H(n,\gamma)^{2}H$ capture reactions; see table 1).

Lastly, the contribution to the blood dose from scattered secondary radiation from the surrounding shielding was assessed using MCNP6. The tubes were housed in a computer-driven holder divided by neutron-absorbing boron−aluminium alloy plates, the whole enclosed in borated polyethylene shielding. Simulations were performed in which an individual blood tube was placed between two boron−aluminum plates. The blood tube was subjected to the scattered neutron beam and it was found, using tally tagging techniques, that the secondary gamma rays arising from (n, γ) capture reactions in the plates delivered a negligible kerma per unit incident neutron fluence through blood. Specifically, the values were 6.96×10^{-5} and 6.67×10^{-5} pGy cm^2 n^{-1} for the PG crystal and super mirror respectively. These values are four orders of magnitude lower than that due to $^{14}N(n,p)^{14}C$ and $^{1}H(n,\gamma)^{2}H$ capture reactions in blood (table 1).

3. Dosimetry for irradiated blood samples

The main purpose of these MCNP6 simulations was to determine the effectiveness of rotating the blood tubes in establishing a uniform thermal neutron dose profile. Two additional sets of MCNP6 simulations were performed to determine the kinetic energy released per unit mass (kerma) delivered to the overall blood volume by secondary gamma rays. Note that cross sections from the .80c library were used for these simulations.

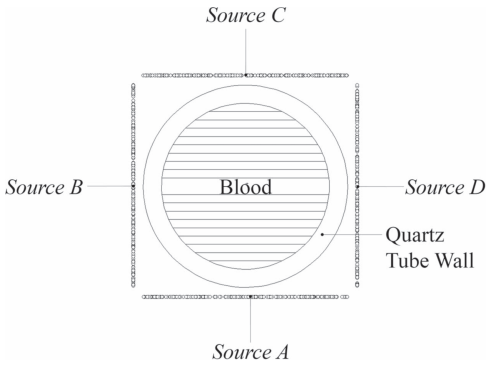

Figure 6. Overhead view of four neutron sources illustrating, using the MCNP Visual Editor [12], the incident neutrons, their spatial starting points, and the partitioning of blood volume. The blood tube holder was surrounded by a void. Neutrons were emitted normal from each planar source.

3.1. Thermal neutron dose profile in blood

The blood volume was divided into 19 vertical segments, each with an average width of 0.525 mm. To demonstrate the need to rotate the blood samples, simulations were first performed, in which the quartz tube and blood volume were irradiated by a single planar neutron source of width 12.8 mm and height 50 mm to simulate stationary irradiation (illustrated as Source A in figure 6). To prove the viability of rotational irradiation in establishing a uniform dose profile, the quartz tube and blood volume were surrounded and simultaneously irradiated by four of the aforementioned planar sources (illustrated as Sources A−D in figure 6).

The MCNP6 F4 tally along with an FM4 tally modifier was used to calculate the number of $^{14}N(n,p)^{14}C$ capture reactions that take place in each segment divided by the volume of the segment. Each capture reaction results in the emission of a 584 ± 3 keV secondary proton and a 41.87 keV ^{14}C residual nucleus [13]. Their energy was deposited locally due to the range of the proton and residual nucleus in blood being approximately 10 μm and 0.19 μm respectively [14]. Therefore, for this neutron capture reaction, that lead to the emission of secondary charged particles and residual nuclei, the kerma in the blood volume was equal to the absorbed dose. The dose profiles on entering the blood volume for both the super mirror and PG crystal, for the stationary irradiation mode, showed an expected build-up in absorbed dose and then a decreasing trend moving through the blood (figure 7).

The rotation of the blood tube during irradiation was effective in providing uniform dose delivery throughout the blood volume (figure 7). The spatial distribution of absorbed dose in blood was greater in amplitude and flatter across the blood volume for the super mirror than for the PG crystal. In addition, the mean value of each of the four depth-dependent dose-per-unit fluence curves shown in figure 7 for both PG crystal and super mirror represented a 5% −8% change to the earlier analytically calculated values of 0.18 pGy cm^2 n^{-1} and 0.25 pGy cm^2 n^{-1} respectively, derived from figures 3 and 5. For comparison, Schmid *et al* [15] calculated an absorbed dose per unit fluence delivered to a blood volume, by 25.3 meV neutrons, to be 0.26 pGy cm^2 n^{-1} (excluding secondary gamma contributions). However, this value used a 3.30% ^{14}N mass fraction in blood—as opposed to the 2.96% value used in this study [10]. Using the latter mass fraction, the value reported from Schmid *et al* [15] becomes 0.23 pGy cm^2 n^{-1}.

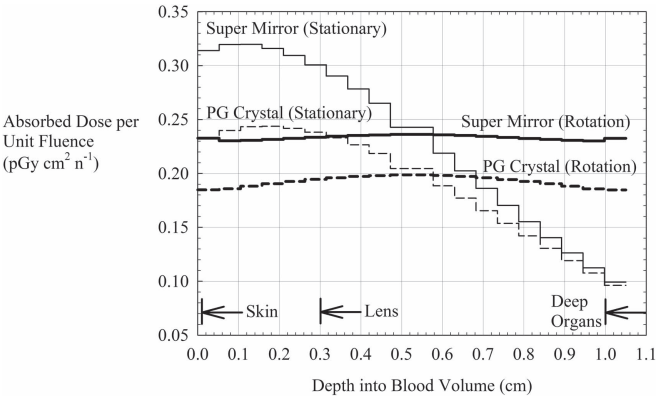

Figure 7. Spatial distribution of absorbed dose from ^{14}N(n,p)^{14}C delivered to blood segments per unit neutron fluence through overall blood volume. The target depths of skin, lens, and deep organs are shown.

A pertinent point is that blood and soft tissue consist mainly of hydrogen-1, natural carbon isotopes, oxygen-16, and nitrogen-14, and that the mass fractions of each of these isotopes are similar in both materials [10]—their mass fraction in blood being 10.19% ^{1}H, 10.00% ^{nat}C, 2.96% ^{14}N, and 75.94% ^{16}O and their mass fraction in soft tissue (International Commission on Radiation Units and Measurements (ICRU) Four Component), 10.12% ^{1}H, 11.10% ^{nat}C, 2.60% ^{14}N, and 76.18% ^{16}O. This near equivalency between blood and soft tissue assists in the interpretation of the data presented from this point on. For example, the spatial absorbed dose distributions shown in figure 7 are approximately equal to those in soft tissue whose physical shape and extents as well as mass are identical to the blood volume described earlier.

Lastly, as an aside, nominal doses to the skin, eye lenses, and deep organs were evaluated by an antero-posterior irradiation incident on blood and considering target depths as recommended by the International Commission on Radiological Protection (ICRP) Publication 103 [16]. These frontal organs have a thermal neutron dose profile as shown in figure 7 due to the ^{14}N(n,p)^{14}C reaction only. With respect to radiation-induced cataractogenesis, the simulations show a build-up of absorbed dose from the cornea peaking at 1–2 mm—thus, occurring before the lens target at 3 mm (considered the radiosensitive target depth for cataracts [17]).

3.2. Secondary gamma ray kerma to blood

The first set of two additional MCNP6 simulations quantified the kerma delivered to the blood by secondary gamma rays produced from (n,γ) capture reactions in the quartz tube wall and from radiative capture reactions with ^{1}H nuclei in blood. There were two approaches: the first based on enabling secondary photon transport and calculating the kerma it delivered to the blood volume; and the second, on enabling secondary photon and tertiary electron transport and calculating the tertiary electron absorbed dose (table 1). The secondary gamma ray kerma per unit fluence and the tertiary electron absorbed dose per unit neutron fluence were respectively 67% and 42% that of the neutron absorbed dose per unit neutron fluence. The percentage associated with tertiary electrons was significantly lower than that pertaining to secondary gamma rays. The former quantity accounted for only the energy deposited by tertiary electrons in the blood volume (4.33 cm^3), while the latter accounted for the energy

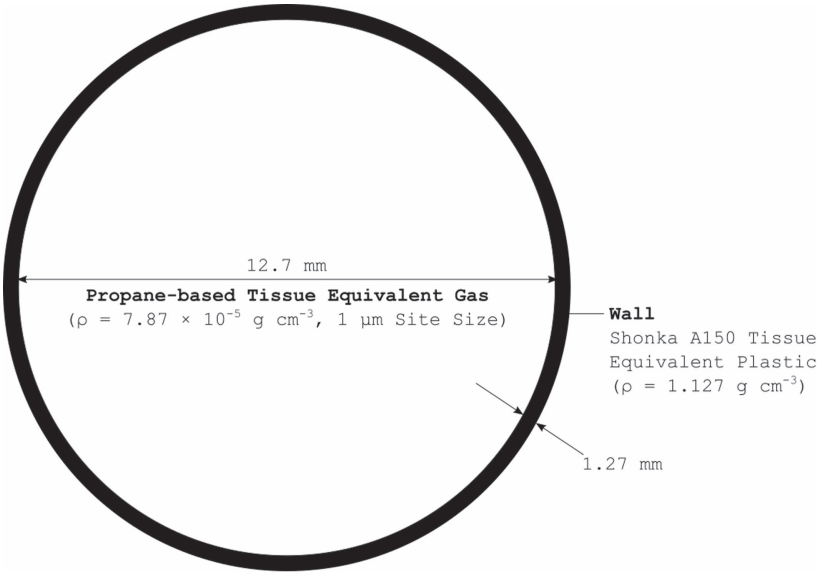

Figure 8. Illustration of half-inch TEPC design parameters employed in PHITS[6] simulations.

imparted to tertiary electrons by secondary gamma rays. Schmid *et al* reported that the absorbed dose to a smaller blood volume of 0.70 cm^3 by secondary gamma rays released from the $^{1}H(n,\gamma)^{2}H$ capture reactions was 28% that due to the $^{14}N(n,p)^{14}C$ neutron capture reaction. Therefore, the percentage of the total dose contributed by tertiary electrons was target-volume-dependent.

The second set of additional MCNP6 simulations quantified the kerma exclusively from secondary gamma rays produced by (n,γ) capture reactions in the quartz tube wall alone, of thickness 0.115 cm and composed of $^{28}Si^{16}O_2$ (^{28}Si and ^{16}O have mass fractions of 46.74% and 53.26% respectively [10]). When the $^{28}Si(n,\gamma)^{29}Si$ and $^{16}O(n,\gamma)^{17}O$ reactions occur in the quartz tube wall, 8.47 MeV [18] and 4.15 MeV [18] secondary gamma rays were emitted from the $(^{29}Si)^*$ and $(^{17}O)^*$ metastable nuclei, respectively, with equal probability. The secondary gamma ray kerma delivered to the blood volume per unit neutron fluence was calculated to be 9.98 fGy cm^2 n^{-1} and 12.82 fGy cm^2 n^{-1} when using the PG crystal and super mirror respectively. The secondary gamma ray kerma was 5.5% and 5.1% of the corresponding rotational neutron absorbed dose per unit fluence respectively listed above. This conservative estimate assumed that all tertiary electrons and positrons created in the blood volume by secondary gamma rays deposited their entire kinetic energy within the blood volume. This analysis determined that the dose contribution to blood from secondary gamma rays emanating from the quartz wall was comparatively small.

4. Microdosimetric characterisation of thermal neutron beams

The microdosimetric nature and mean quality factor of the thermal neutrons incident on the blood sample, with spectra as shown in figures 3 and 5, was characterised by simulating, using PHITS, the response of a half-inch tissue equivalent proportional counter (TEPC) identical to that manufactured by Far West Technology, Inc. [19] (figure 8). PHITS was

employed because of its unique event generator capability, which enables the transport of secondary particles produced from neutron capture interactions [7]. Inherent approximations and uncertainties were associated with the use of a TEPC for microdosimetry investigations—specifically, the ability of tissue equivalent gas and plastic to adequately represent soft tissue, arbitrary choice of simulated microscopic tissue site diameter, and the interpretation of insider, starter, and crosser events. Nevertheless, the thermal neutron mean quality factor calculated using the TEPC-based framework can be directly compared to that measured by an exposed TEPC. An alternative method, not carried out in this study, is to calculate the mean quality factor by first determining the secondary charge particle kinetic energy deposition spectrum in the blood sample; however, no physical measurements of this quantity are available for comparison.

The aforementioned half-inch TEPC instrument consisted of a 12.7 mm diameter sensitive gas volume and a 1.27 mm thick wall. The TEPC wall was composed of Shonka A150 tissue equivalent plastic with a density of 1.127 g cm^{-3} [10]. This TEPC was chosen as its small dimensions fit within the scattered neutron field incident on the blood sample (figures 2 and 4). The sensitive gas volume was filled with propane-based tissue equivalent gas at a density of 7.87 $\times$ 10^{-5} g cm^{-3}, to simulate a 1 μm diameter microscopic tissue volume. The sensitivity constant of this instrument, accounting for the mean chord length of the simulated site and mass of gas in the sensitive volume, was determined to be 787 keV μm^{-1} μGy^{-1}. Note that in propane-based tissue equivalent gas and Shonka A150 tissue equivalent plastic, the ^{14}N mass fraction is 3.50% [10]—which differs from that in blood and soft tissue mentioned earlier. Nevertheless, as the $^{14}N(n,p)^{14}C$ capture reaction is the dominant contributor to dose delivered to biological media by thermal neutrons, this difference in ^{14}N mass fraction will not significantly impact the estimation of quality factor.

Using cross sections from the .50c library, the TEPC was irradiated by an expanded and aligned planar neutron field, and the transport of secondary protons (cut off = 10^{-9} MeV), secondary alpha (cut off = 10^{-9} MeV u^{-1}), secondary heavy recoil and residual nuclei (cut off = 10^{-9} MeV u^{-1}) were enabled along with secondary gamma rays (cut off = 10^{-3} MeV) and tertiary electrons and positrons (cut off = 10^{-3} MeV). The production and transport of secondary and tertiary particles were enabled by declaring parameters e-mode = 1 and igamma = 1. The T-Track and T-Deposit tallies were used to calculate the primary neutron fluence through the TEPC and the pulse heights of energy deposition events in the sensitive gas volume respectively. Using these pulse heights, dose distributions for all energy depositing particles as well as tertiary electrons and positrons were calculated and normalised both to the total absorbed dose delivered by all secondary and tertiary charged particles (figures 9 and 10 for PG crystal and super mirror respectively) and also to lineal energy logarithmic bin width. Note that in these figures, the left vertical axis pertains to all secondary and tertiary charged particles; the right vertical axis, to tertiary electrons and positrons.

The dominant contribution of high lineal energy events (dose mean lineal energy = 67 keV μm^{-1}, table 2) are due to secondary protons and residual ^{14}C nuclei produced by the $^{14}N(n,p)^{14}C$ capture reaction (figures 9 and 10). Also shown is that the low linear energy transfer (LET) tertiary electron and positron contribution to the total dose is small, being 3.94% and 3.71% for the PG crystal and super mirror respectively, and that their dose distributions have a sharp drop-off beyond 10 keV μm^{-1}.

ICRP 103 [16] and ICRP 21 [20] provide different guidance on how the quality factor varies with LET. ICRP 103 states that the quality factor continuously increases in value up to 100 keV μm^{-1}, at which point its value is 30, and then steadily decreases in value beyond 100 keV μm^{-1}. In contrast, ICRP 21 states that the quality factor steadily increases in value

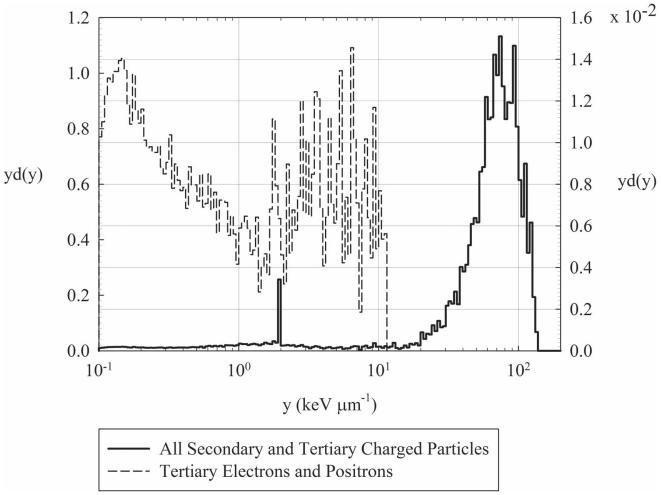

Figure 9. Dose distributions versus lineal energy measured by ½-inch TEPC when PG crystal is inserted into incident thermal neutron beam line.

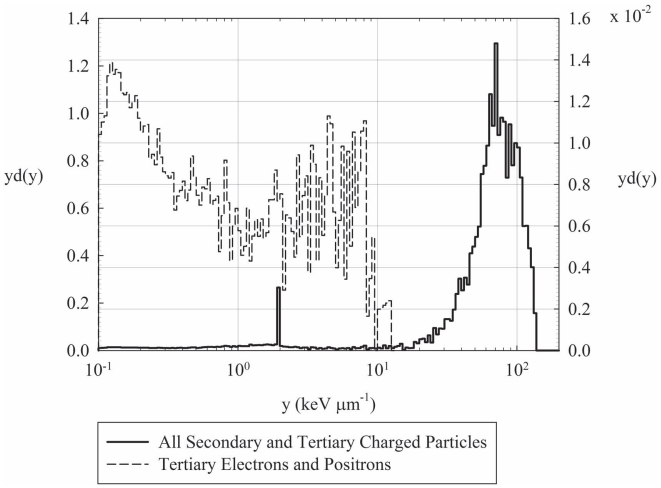

Figure 10. Dose distributions versus lineal energy measured by ½-inch TEPC when super mirror is inserted into incident thermal neutron beam line.

up to 150 keV μm^{-1}, at which point its value is 20, and then maintains a value of 20 up to 1000 keV μm^{-1}.

Alberts *et al* [21] exposed a half-inch TEPC, simulating a 1 μm site size, to a thermal neutron beam of unspecified kinetic energy. Using ICRP 21 guidelines, a dose equivalent per unit neutron fluence of 4.2 pSv cm^2 n^{-1} was reported for the instrument. Table 2 shows that from the PHITS simulation, the calculated dose equivalent per unit neutron fluence through the TEPC using ICRP 21 guidelines, when exposed to the scattered neutron energy spectrum using the super mirror was 3.80 ± 0.44 pSv cm^2 n^{-1}—similar to the value measured by Alberts *et al*. This establishes confidence in the PHITS simulation model.

Table 2. Microdosimetric response parameters estimated for the half-inch TEPC instrument.

Response metric	Scattering element	
	PG crystal	Super mirror
Frequency mean lineal energy (keV μm^{-1})	6.44 ± 0.19	6.74 ± 0.18
Dose mean lineal energy (keV μm^{-1})	66.17 ± 2.96	68.60 ± 2.74
Dose equivalent per unit neutron fluence (pSv cm^2 n^{-1}) (ICRP 21) [20]	2.85 ± 0.15	3.80 ± 0.44
Dose equivalent per unit neutron fluence (pSv cm^2 n^{-1}) (ICRP 103) [16]	4.71 ± 0.25	6.29 ± 0.29
Ambient dose equivalent per unit neutron fluence (pSv cm^2 n^{-1}) (ICRP 103) [16]	11.76	10.62
Dose equivalent response (ICRP 103) [16]	0.40 ± 0.02	0.59 ± 0.03
Sensitivity (counts μSv^{-1}) (ICRP 21) [20]	10.95 ± 0.57	10.20 ± 0.47
Sensitivity (counts μSv^{-1}) (ICRP 103) [16]	6.64 ± 0.35	6.16 ± 0.29
Mean quality factor (ICRP 21) [20]	11.16 ± 0.48	11.46 ± 0.44
Mean quality factor (ICRP 103) [16]	18.42 ± 0.82	18.98 ± 0.75

Accounting for the scattered neutron energy spectrum incident on the blood samples and ICRP 103 [16] guidelines, when the PG crystal was used, the ambient dose equivalent per unit of neutron fluence was 11.76 pSv cm^2 n^{-1}; and when the super mirror was employed, 10.62 pSv cm^2 n^{-1}. When the PG crystal and super mirror were used, the corresponding simulated dose equivalent response of the half-inch TEPC was evaluated as 0.40 ± 0.02 and 0.59 ± 0.03 respectively (table 2).

The high quality factors measured by the TEPC using ICRP 103 guidelines—18.42 ± 0.82 when a PG crystal was used and 18.98 ± 0.75 when a super mirror was used—compared well to the neutron quality factor of 19.17, for 25.3 meV incident neutrons, calculated by Schuhmacher and Siebert [22] at a point 10 mm within the ICRU tissue sphere [23] of 30 cm diameter, using the relationship between quality factor and LET from ICRP 60 [24]. The 19.17 quality factor only accounts for neutron interactions which lead to the emission of heavy charged particles, viz. from $^{14}N(n,p)^{14}C$ capture. For comparison, ICRP 103 listed the thermal neutron radiation weighting factor to be 2.5, and accounted for thermal neutrons undergoing both the $^{1}H(n,\gamma)^{2}H$ and $^{14}N(n,p)^{14}C$ capture reactions in soft tissue [16].

Paterson [4] exposed blood to thermal neutrons and reported a relative biological effectiveness (RBE), using the 'maximum RBE method' iteratively re-weighted least squares linear regression method [25], of 26 ± 7 for a biological end point of dicentric chromosome induction. A few animal studies have also indicated high RBE values for thermal-neutron-induced cataracts, including a value of 10.2 by Harris [26]. These large RBE values were due to the dominant contributor to the thermal neutron absorbed dose being the $^{14}N(n,p)^{14}C$ reaction, which produced high LET products having a large microdosimetric quality factor of 19, as determined from the PHITS simulations. In the simulated TEPC, the dominant contributor to the absorbed dose delivered to the sensitive gas volume was the $^{14}N(n,p)^{14}C$ reaction, and each of these reactions resulted in a secondary proton and residual ^{14}C pair producing large lineal energy events in the gas, with the consequence that a high quality factor of approximately 19 was measured in the TEPC. The relatively low mass of ^{1}H in the TEPC instrument (0.0889 g) resulted in the $^{1}H(n,\gamma)^{2}H$ reaction contributing approximately 4% to the absorbed dose delivered to the gas, further enabling the TEPC to measure a high mean microdosimetric quality factor for thermal neutrons.

Table 3. Kerma delivery metrics for 3 mm and 10 mm depths into ICRU sphere, targets of the lens of the eye and deep organs respectively, summing thermal neutron and secondary gamma contributions[a].

Quantity	PG crystal		Super mirror	
	3 mm	10 mm	3 mm	10 mm
Total kerma from $^{14}N(n,p)^{14}C$ and $^{1}H(n,\gamma)^{2}H$ per unit neutron fluence (pGy cm^2 n^{-1})	2.28	2.86	2.50	2.65
Dose equivalent per unit incident neutron fluence (pSv cm^2 n^{-1})	11.62	12.88	13.00	12.52
Percent of total kerma from $^{1}H(n,\gamma)^{2}H$ (%)	77.44	80.72	76.94	79.56

[a] No value was calculated for a target point at 0.07 mm due to inadequate statistics.

The abundance of thermal neutrons in neutron fields present in a variety of environments, such as nuclear power plant workplaces [1], radiotherapy environments [2], and high altitudes [3] or space, necessitates the study of the ability of thermal neutrons to induce biological damage. The observation that biological changes due to thermal neutron exposure arises from high LET events from the $^{14}N(n,p)^{14}C$ reaction (figures 9 and 10) is relevant with regard to understanding the contribution that thermal neutrons make in inducing biological damage in diverse environments, such as cataract induction in astronauts [27, 28] and in the induction of secondary cancer in patients from a secondary neutron field when undergoing high energy radiation therapy [29].

5. Relevance of blood irradiations to dosimetry of eye lens and other targets

The PHITS microdosimetry results have shown that, even in the absence of significant secondary gamma ray fields, thermal neutrons are capable of inducing biological damage due to the subsequent high LET secondary particles that traverse blood and tissue media. For an antero-posterior irradiation by incident thermal neutrons, frontal organs—namely, the skin and eye lenses (respectively located 0.07 mm and 3 mm from the surface of the body)—are prone to more biological damage than deeper organs, as the high LET particles produced make a greater contribution to the total absorbed dose compared to secondary gamma rays.

This was best demonstrated by MCNP6 simulations in which an ICRU sphere of 30 cm diameter, made of tissue equivalent material representing the whole body soft tissues, was irradiated by an expanded and aligned neutron field emitting the thermal neutron energy spectra derived from figures 3 and 5. ICRU recommends estimating dose equivalent for superficial organs at depths of 0.07 mm for skin and 3 mm for the lens of the eye; a target depth of 10 mm represents deep organs. Total kerma to targets was simulated by primary neutron and secondary gamma ray transport for target depths of 3 and 10 mm, and the dose equivalent was estimated, as described by Dietze and Siebert [30], for the two target depths from the sum of the kerma delivered by primary neutrons and secondary gamma rays—each weighted with their respective quality factor of 19.17 [22] for neutrons and 1 for gamma rays.

The dose equivalent per unit thermal neutron fluence (pSv cm^2 n^{-1}) decreased at about 20% and 6% for PG crystal and super mirror use respectively when comparing targets at 10 mm and 3 mm (table 3). Booz [31] and Dietze and Siebert [30] report that for incident neutrons of kinetic energy 1 eV and below, the contribution to the total absorbed dose delivered by secondary gamma rays to the 10 mm point is approximately 80%, which was in

good agreement with the percentages listed in table 3. In addition, the dose equivalent per unit neutron fluence at the 10 mm point were close to the corresponding ambient dose equivalent per unit fluence on the blood sample values reported earlier of 11.76 pSv cm^2 n^{-1} and 10.62 pSv cm^2 n^{-1} when the PG crystal and super mirror were used, respectively. For both PG crystal and super mirror use, the fraction of the total kerma from secondary gamma rays at the 3 mm target was slightly lower than that at the 10 mm target (table 3). This indicates that as the target point moved closer to the surface of the body, the contribution of secondary gamma rays to the total kerma decreased.

The gamma component of the total thermal neutron dose was dependent on the depth of the target (figure 7) within an irradiated volume and the mass of ^{1}H in the irradiated volume. This gamma component increased with mass of ^{1}H in the irradiated volume, specifically 4% in the TEPC of 0.0889 g, 22% and 29% in blood volumes of 0.70 cm^3 [15] and 0.468 g (this study), and 77%-81% in the larger ICRU sphere (1430 g). This was also confirmed by Dietze and Siebert [30], who found that a decreasing fraction of the total absorbed dose from secondary gamma rays was delivered to tissue phantoms of decreasing size. Thus, the low LET events derived from the small ^{1}H mass in the TEPC resulted in high LET $^{14}N(n,p)^{14}C$ events dominating the dose delivered and analysed, consequently enabling measurement of high quality factor secondary particle species.

6. Conclusions and future work

Radiobiology studies focusing on the thermal neutron irradiation of blood have been ongoing at the NRU reactor. This study used three Monte Carlo simulation codes to characterise these irradiations. The McStas code calculated the spatial size and wavelength distributions of thermal neutrons incident at the blood sample placement point when a PG crystal and super mirror were used in the incident beam line emanating from NRU.

It was shown using the MCNP6 code that spinning each blood tube results in the spatial absorbed dose distribution from $^{14}N(n,p)^{14}C$ reactions in blood to be more uniform. The $^{14}N(n,p)^{14}C$ reaction contributes approximately 71% of the total absorbed dose to the blood, while the remaining 29% is due to tertiary electrons liberated by secondary gamma rays emanating from the quartz wall and blood (table 1). This 29% value compares to the 77%–81% contribution to the total kerma delivered to the 3 mm (eye lens) and 10 mm (deep organs) target points internal to the ICRU sphere by secondary gamma rays from $^1H(n,\gamma)^2H$ (table 3). It is acknowledged that these values may be impacted by the limited accuracy of MCNP6 version 1.0 in modelling secondary gamma ray emission for thermal neutron capture with hydrogen-1.

This target-dimension-dependence of the low LET component (from secondary gamma rays and tertiary electrons) influences the calculation of the overall quality factor and subsequent RBE for thermal neutrons, as they are dependent on the frequency of high LET (from $^{14}N(n,p)^{14}C$) and low LET events occurring in the irradiated medium. In summary, it was found that the gamma component of the thermal neutron dose increases with target volume, which has implications for animal and human exposure studies. Consequently, dosimetric calculations to smaller eye lenses in mice will yield a higher quality factor than that determined from corresponding human exposures.

Using the PHITS code, a microdosimetric quality factor of about 19 was estimated for thermal neutrons initiating the $^{14}N(n,p)^{14}C$ reaction in tissue. Dicentric chromosome induction in lymphocytes in blood induced by thermal neutrons yielded an RBE value of 26 $\pm$ 7 [4]. This large RBE value can be attributed to the $^{14}N(n,p)^{14}C$ reaction, producing high LET

products, being the dominant contributor to the absorbed dose to blood and its corresponding high microdosimetric quality factor. For antero-posterior irradiation, frontal organs experience an abundance of high LET events and consequently a large mean quality factor, which can contribute to the formation of cataracts and perhaps certain cancers.

This theoretical, microdosimetric confirmation of a high quality factor for the $^{14}N(n,p)^{14}C$ reaction initiated by thermal neutrons has important implications, such as whether nuclear or mitochondrial damage is paramount. Doubts arise as to the overall dominant role of nuclear damage from knowing that 1 mGy of x-ray radiation produces double strand breaks (DSBs) in only ~3% of cells, yet 20–80 DSBs lead to cell death [32, 33]. In light of the premise that low LET radiation is more likely associated with indirect rather than direct nuclear damage (for example, arising from mitochondrially derived reactive oxygen species [34]), this contrasts with the effects of high LET radiation linked to direct damage to nuclear DNA and resulting genomic instability. Therefore, the high LET component of thermal neutron exposures may have the potential, relative to low LET radiation to induce different detrimental health effects when in reactor, radiotherapy, and space environments.

Acknowledgments

This work was supported by the Atomic Energy of Canada Limited Federal Nuclear Science and Technology Work Plan. The authors would like to acknowledge Dr John Root, Director of the Canadian Neutron Beam Centre, for his support of this study, and thank the individuals that contributed blood samples used for thermal neutron irradiations at NRU. The authors declare no conflict of interest.

ORCID iDs

J Kildea https://orcid.org/0000-0002-7084-1425

References

[1] Nunes J C, Cross W G and Waker A J 1997 Feasibility of creating 'Candu®-Like' workplace neutron fields in an existing irradiation facility *Radiat. Prot. Dosim.* **72** 11–20
[2] Maglieri R, Licea A, Evans M, Seuntjens J and Kildea J 2015 Measuring neutron spectra in radiotherapy using the nested neutron spectrometer *Med. Phys.* **42** 6162–9
[3] Goldhagen P, Clem J M and Wilson J W 2004 The energy spectrum of cosmic-ray induced neutrons measured on an airplane over a wide range of altitude and latitude *Radiat. Prot. Dosim.* **110** 387–92
[4] Paterson L 2016 Low dose effects of gamma and neutron radiation on peripheral blood lymphocytes *McMaster University Thesis* Hamilton, ON
[5] McStas—A neutron ray-trace simulation package. Accessed April 2016 at (http://mcstas.org/)
[6] Pelowitz D B 2013 MCNP6™ User's Manual Version 1.0. LANL Report LA-CP-13-00634 Rev. 0. Los Alamos National Laboratory
[7] Sato T *et al* 2013 Particle and heavy ion transport code system PHITS, version 2.52 *J. Nucl. Sci. Technol.* **50** 913–23
[8] Cember H 1996 *Introduction to Health Physics* 3rd edn (New York: McGraw-Hill)
[9] National Nuclear Data Center. Q-value Calculator (QCalc). Accessed February 2017 at (http://nndc.bnl.gov/qcalc/)
[10] Pacific Northwest National Laboratory 2011 Compendium of Material Composition Data for Radiation Transport Modeling. PIET-43741-TM-963, PNNL-15870 Rev. 1. PNNL

[11] Pynn R 2009 Chapter 2: neutron scattering—a non destructive microscope for seeing inside matter ed L Liang *et al Neutron Applications in Earth, Energy, and Environmental Sciences* (New York: Springer) pp 15–36
[12] Schwarz A L, Schwarz R A and Carter L L 2011 MCNP/MCNPX Visual Editor Computer Code Manual. Visual Editor Consultants
[13] Bethe H A 1950 The range-energy relation for slow alpha-particles and protons in air *Rev. Mod. Phys.* **22** 213–9
[14] SRIM—Stopping and Range of Ions in Matter. Accessed March 2017 at (http://srim.org/)
[15] Schmid E, Wagner F M, Canella L, Romm H and Schmid T E 2013 RBE of thermal neutrons for induction of chromosome aberrations in human lymphocytes *Radiat. Environ. Biophys.* **52** 113–21
[16] International Commission on Radiological Protection 2007 The 2007 Recommendations of the International Commission on Radiological Protection. ICRP Publication 103. ICRP
[17] Charles M W and Brown N 1975 Dimensions of the human eye relevant to radiation protection *Phys. Med. Biol.* **20** 202–18
[18] Groshev L V, Demidov A M, Lutsenko V N and Pelekhov V I 1959 *Atlas of γ-Ray Spectra from Radiative Capture of Thermal Neutrons* (Oxford: Pergamon)
[19] Far West Technology, Inc. LET-1/2, 0.5″ TE PROPORTIONAL COUNTER. Accessed March 2017 at (http://fwt.com/detector/let1_2ds.htm)
[20] International Commission on Radiological Protection 1973 Data for Protection Against Ionizing from External Sources—Supplement to ICRP Publication 15. ICRP Publication 21. ICRP
[21] Alberts W G, Bühler G, Dudler R, Menzel H G and Schuhmacher H 1984 Experimental study of the dose equivalent response of tissue-equivalent proportional counters to low energy neutrons *Radiat. Prot. Dosim.* **9** 211–4
[22] Schuhmacher H and Siebert B R L 1992 Quality factors and ambient dose equivalent for neutrons based on the new ICRP recommendations *Radiat. Prot. Dosim.* **40** 85–9
[23] International Commission on Radiation Units and Measurements 1980 Radiation Quantities and Units. ICRU Report 33. ICRU
[24] International Commission on Radiological Protection 1991 1990 Recommendations of the International Commission on Radiological Protection. ICRP Publication 60. ICRP
[25] International Atomic Energy Agency 2011 Cytogenic Dosimetry: Applications in Preparedness for and Response to Radiation Emergencies. IAEA
[26] Harris P S 1954 Measurement of slow neutrons and coexisting radiations *Radiat. Res.* **1** 34–42
[27] Chylack L T Jr, Peterson L E, Feiveson A H, Wear M L, Manuel F K, Tung W H, Hardy D S, Marak L J and Cucinotta F A 2009 NASA study of cataract in astronauts (NASCA). Report 1: cross-sectional study of the relationship of exposure to space radiation and risk of lens opacity *Radiat. Res.* **172** 10–20
[28] Hamada N and Sato T 2016 Cataractogenesis following high-LET radiation exposure *Mutat. Res.* **770** 262–91
[29] Kry S F, Howell R M, Salehpour M and Followill D S 2009 Neutron spectra and dose equivalents calculated in tissue for high-energy radiation therapy *Med. Phys.* **36** 1244–50
[30] Dietze G and Siebert B R L 1994 Short communication—photon and neutron dose contributions and mean quality factors in phantoms of different size irradiated by monoenergetic neutrons *Radiat. Res.* **140** 130–3
[31] Booz J 1984 Advantages of introducing microdosimetric instruments and methods into radiation protection *Radiat. Prot. Dosim.* **9** 175–83
[32] Rothkamm K and Lobrich M 2003 Evidence for a lack of DNA double-strand break repair in human cells exposed to very low x-ray doses *Proc. Natl Acad. Sci. USA* **100** 5057–62
[33] Radford I R 1985 Evidence for a general relationship between the induced level of DNA double-strand breakage and cell-killing after X-irradiation of mammalian cells *Int. J. Radiat. Biol. Relat. Stud. Phys. Chem. Med.* **49** 611–20
[34] Richardson R B and Harper M E 2016 Mitochondrial stress controls the radiosensitivity of the oxygen effect: implications for radiotherapy *Oncotarget.* **7** 21469–83